Gravitatonal wave sources and multi-messenger gravitatonal wave astrophysics

Hideyuki TAGOSHI
Institute for Cosmic Ray Research
The University of Tokyo

Synergies at New Frontiers
at Gamma Rays, Neutrinos and Gravitational Waves
ICRR, March 24-25, 2022

Contents

- Sources of gravitational waves (GW)
- Core collapse supernovae GW
- BNS and sky localization
- Low latency alert

Emission of gravitational waves

- Emission of strong gravitational waves requires
  - Non spherically symmetric motion of mass
  - Motion should be very high speed ⇔ strong self-gravity
    - Compact objects are main sources (BH, NS, WD, ...)

- Gravitational wave sources
  - Compact binary coalescence (CBC) (BH-BH, NS-BH, NS-NS)
  - Steller core collapse (burst waves)
  - Pulsar (continuous waves)
  - ......

Core Collapse Supernova GW

Neutrino-driven mechanism

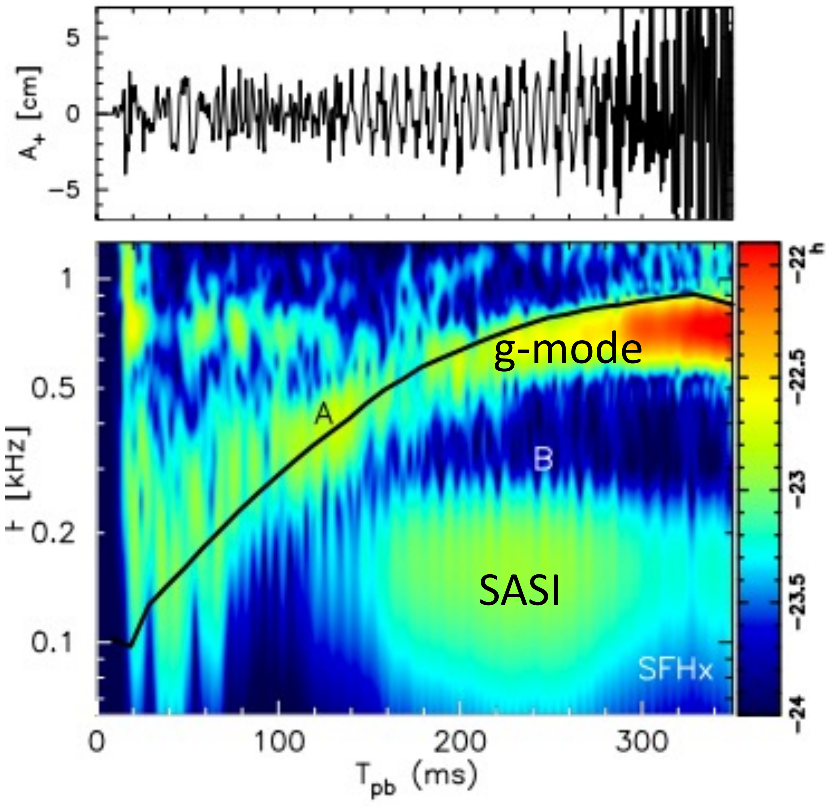

Kuroda et al. ApJ 829, L14 (2016)

(Rapidly rotating progenitor model)
Magnetorotationally-driven (MHD-driven) mechanism

core boune

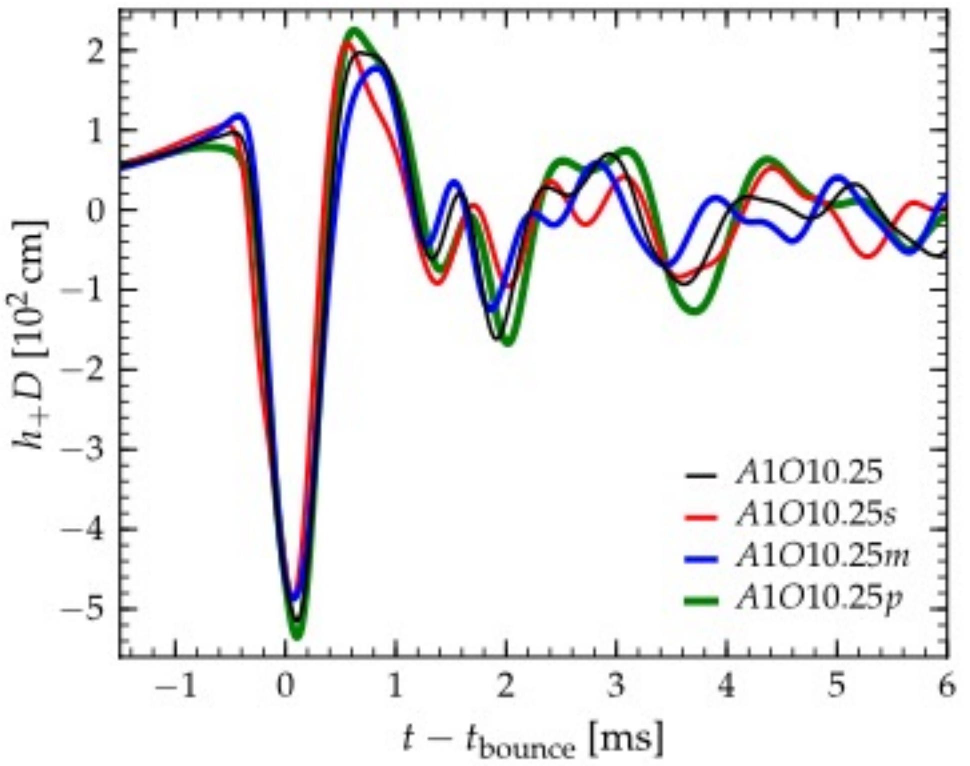

Abdikamalov et al. PRD90, 044001 (2014)

Detectability of Core Collapse Supernova GW

M.J. Szczepańczyk et al. arXiv:2104.06462

TABLE I. Waveforms from multidimensional CCSN simulations described in the text. For each waveform family we provide a reference, dimensionality, a summary of the numerical method (EOS and code name) and observed GW features. Then, we provide details for example waveforms: identifier, progenitor stellar mass $M_{\rm star}$, initial central angular velocity Ω_c, the frequency $f_{\rm peak}$ at which the GW energy spectrum peaks, the emitted GW energy E_{GW} and approximate signal duration. The superscript symbols: †non-ZAMS, *the simulation was stopped before the full GW signal was developed.

Waveform Family	Numerical Method	GW Features	Waveform Identifier	$M_{\rm star}$ [$M_\odot$]	Ω_c [rad/s]	$f_{\rm peak}$ [Hz]	$E_{\rm GW}$ [$M_\odot c^2$]	Duration [ms]
Abdikamalov et al. 2014, 2D [76]	LS220, Shen CoCoNuT	bounce prompt-conv.	A1O01.0	12	1.0	819	9.4×10^{-9}	50*
			A2O01.0	12	1.0	854	1.7×10^{-8}	50*
			A3O01.0	12	1.0	867	7.0×10^{-9}	50*
			A4O01.0	12	1.0	873	4.2×10^{-9}	50*
Andresen et al. 2017, 3D [51]	LS220 CoCoNuT PROMETHEUS	g-modes SASI (spiral) convection	s11	11.2	-	642	1.1×10^{-10}	350*
			s20	20	-	687	7.4×10^{-10}	430*
			s20s	20	-	693	1.4×10^{-9}	530*
			s27	27	-	753	4.4×10^{-10}	570*
Andresen et al. 2019, 3D [77]	LS220 PROMETHEUS	SASI (spiral) g-modes	m15fr	15	0.5	689	2.7×10^{-10}	460*
			m15nr	15	-	820	1.5×10^{-10}	350*
			m15r	15	0.2	801	7.1×10^{-11}	380*
Cerdá-Durán et al. 2013, 2D [59]	LS220 CoCoNuT	BH formation g-modes, SASI/conv.	fiducial	35	2.0	922	3.3×10^{-7}	1620
			slow	35	1.0	987	9.4×10^{-7}	1050
Dimmelmeier et al. 2008, 2D [78]	LS, Shen CoCoNuT	bounce prompt-conv.	s15A2O09-ls	15	4.6	743	2.7×10^{-8}	60*
			s15A3O15-ls	15	13.3	117	5.2×10^{-9}	340*
			s20A3O09-ls	20	9.0	615	2.2×10^{-8}	80*
Kuroda et al. 2016, 3D [79]	SFHx, DD2, TM1 3D-GR	g-modes SASI	SFHx	15	-	718	2.1×10^{-9}	350*
			TM1	15	-	714	1.7×10^{-9}	350*
Kuroda et al. 2017, 3D [80]	SFHx, DD2, TM1 3D-GR	g-modes SASI/convection	s11.2	11.2	-	195	1.3×10^{-10}	190*
			s15.0	15	-	430	3.1×10^{-9}	210*
Mezzacappa et al. 2020, 3D [73]	LS220 CHIMERA	g-, p-modes SASI/convection	c15-3D	15	-	1064	6.4×10^{-9}	420*
Morozova et al. 2018, 2D [81]	LS220, DD2, SFHo FORNAX	f-, g-, p-modes SASI/convection	M10_LS220	10	-	1594	2.4×10^{-9}	1210
			M10_DD2	10	-	1544	1.7×10^{-9}	1700
			M13_SFHo	13	-	976	1.1×10^{-8}	1360
			M19_SFHo	19	-	1851	6.3×10^{-8}	1540
Müller et al. 2012, 3D [71]	JM PROMETHEUS	SASI/convection	L15-3	15	-	144	2.2×10^{-11}	1400
			N20-2	20	-	147	1.1×10^{-11}	1500
			W15-4	15	-	208	2.5×10^{-11}	1300
O'Connor&Couch 2018, 3D [82]	SFHo FLASH	g-modes SASI/convection	mesa20	20	-	1121	6.3×10^{-10}	500*
			mesa20_LR	20	-	1199	2.2×10^{-9}	650*
			mesa20_pert	20	-	1033	9.5×10^{-10}	530*
			mesa20_v_LR	20	-	887	1.0×10^{-10}	480*
Ott et al. 2013, 3D [83]	LS220 Zelmani	prompt-conv. g-modes	s27-fheat1.00	27	-	836	4.0×10^{-10}	190*
			s27-fheat1.05	27	-	385	3.4×10^{-10}	190*
			s27-fheat1.10	27	-	340	3.3×10^{-10}	190*
			s27-fheat1.15	27	-	839	3.1×10^{-10}	190*
Powell&Müller 2019, 3D [84]	LS220 CoCoNuT-FMT	g-modes	s3.5_pns	$3.5^{\dagger}$	-	878	3.6×10^{-9}	700
			s18	18	-	872	1.6×10^{-8}	890
Powell&Müller 2020, 3D [85]	LS220 CoCoNuT-FMT	f-, g-modes SASI prompt-conv.	s18np	18	3.4	742	7.7×10^{-8}	1000
			m39	39	-	674	7.5×10^{-10}	560
			y20	20	-	872	1.0×10^{-8}	980
Radice et al. 2019, 3D [50]	SFHo FORNAX	f-, g-modes SASI/convection prompt-conv.	s9	9	-	727	1.6×10^{-10}	1100
			s13	13	-	1422	5.9×10^{-9}	800*
			s25	25	-	1132	2.8×10^{-8}	600*
Richers et al. 2017, 2D [86]	18 EOSs CoCoNuT	bounce prompt-conv.	A467_w0.50_SFHx	12	0.5	891	1.6×10^{-8}	60*
			A467_w0.50_LS220	12	0.5	820	5.1×10^{-9}	60*
			A467_w9.50_SFHx	12	9.5	448	4.2×10^{-8}	60*
			A467_w9.50_LS220	12	9.5	863	4.1×10^{-8}	60*
Scheidegger et al. 2010, 3D [54]	LS180 Pen	bounce prompt-conv. convection	R1E1CA_L	15	0.3	1103	1.2×10^{-10}	90*
			R3E1AC_L	15	6.3	588	2.2×10^{-7}	110*
			R4E1FC_L	15	9.4	683	3.9×10^{-7}	100*
Yakunin et al. 2015, 2D [72]	LS220 CHIMERA	g-modes SASI/convection prompt-conv.	B12	12	-	708	3.4×10^{-9}	1300
			B15	15	-	865	7.9×10^{-9}	1100
			B20	20	-	602	4.2×10^{-9}	900
			B25	25	-	1022	1.4×10^{-8}	1140

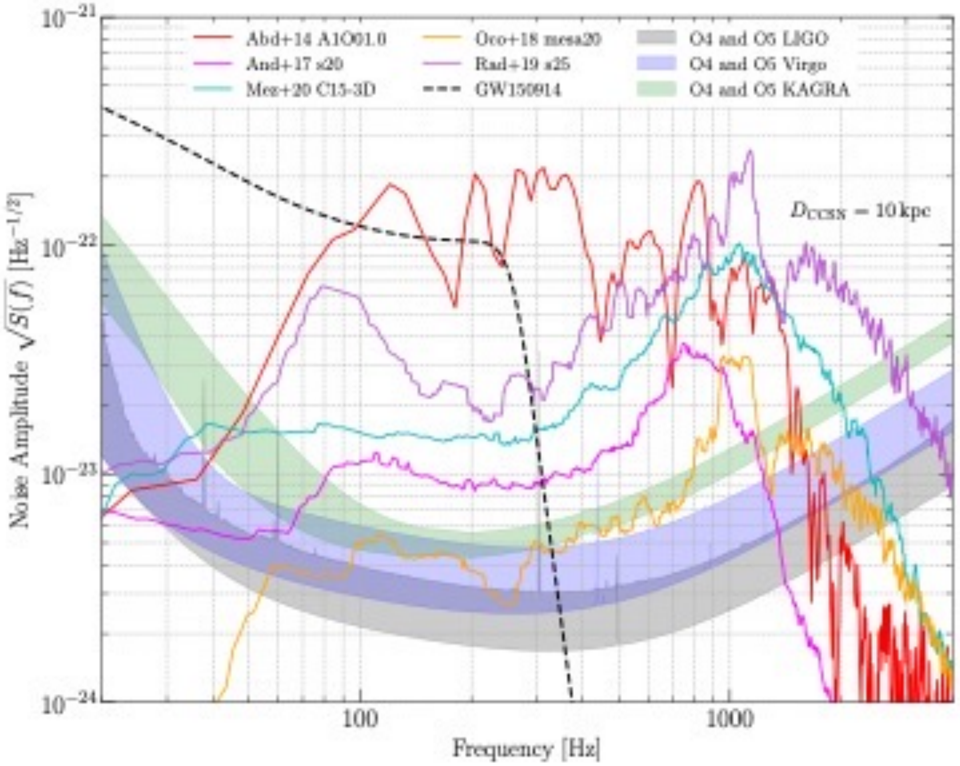

Detection range of Core Collapse Supernova GW

M.J. Szczepańczyk et al. arXiv:2104.06462

TABLE II. The results presenting the sensitivity of cWB to the detection of GWs from a variety of CCSN models. The predicted detection ranges for O4 and O5 are calculated at 10%, 50% and 50% detection efficiency. The detectable SNR is also calculated at 10%, 50% and 90% detection efficiency. The waveform overlap (accuracy of cWB reconstruction) is an averaged at injected SNR of 20, 40 and 60.

Waveform Family	Waveform Identifier	O4 det. range [kpc]			O5 det. range [kpc]			Detect. SNR			Wav. Overlap		
		90%	50%	10%	90%	50%	10%	10%	50%	90%	20	40	60
Abdikamalov et al. 2014 [76]	A1O01.0	NaN	15.9	58.7	NaN	29.4	109.7	9.7	12.7	NaN	0.83	0.90	0.93
	A2O01.0	NaN	19.3	71.0	NaN	35.2	130.0	10.0	13.1	NaN	0.88	0.93	0.94
	A3O01.0	NaN	20.1	84.6	NaN	37.1	157.4	8.9	12.5	NaN	0.86	0.92	0.95
	A4O01.0	NaN	8.4	39.3	NaN	15.2	72.3	10.2	14	NaN	0.88	0.91	0.94
Andresen et al. 2017 [51]	s11	0.6	1.4	2.3	1.1	2.6	4.3	13.1	16.5	25.1	0.59	0.82	0.88
	s20	1.4	3.4	5.6	2.5	6.2	10.4	14.2	17.9	24.9	0.50	0.79	0.88
	s20s	1.6	4.1	6.8	2.9	7.5	12.6	19.7	24.0	35.7	0.35	0.71	0.84
	s27	0.8	1.9	3.1	1.4	3.5	5.7	17.6	22.2	33.5	0.71	0.68	0.83
Andresen et al. 2019 [77]	m15fr	1.4	3.2	5.6	2.5	5.8	10.1	11.4	16.1	22.0	0.61	0.77	0.85
	m15nr	0.8	1.8	3.1	1.4	3.3	5.5	13.0	16.3	22.6	0.59	0.82	0.88
	m15r	0.3	0.9	1.5	0.6	1.6	2.8	16.0	20.0	27.6	0.46	0.78	0.86
Cerdá-Durán et al. 2013 [59]	fiducial	NaN	15.7	51.5	NaN	28.2	93.9	31.0	37.8	NaN	0.52	0.81	0.87
	slow	NaN	35.9	154.3	NaN	66.6	285.7	15.3	19.7	NaN	0.35	0.63	0.81
Dimmelmeier et al. 2008 [78]	s15A2O09-ls	NaN	14.5	60.1	NaN	26.1	117.5	10.2	13.2	NaN	0.86	0.91	0.93
	s15A3O15-ls	NaN	13.6	59.4	NaN	24.5	117.1	9.2	12.8	NaN	0.90	0.94	0.95
	s20A3O09-ls	NaN	12.5	59.9	NaN	22.8	125.9	10.3	14.2	NaN	0.84	0.90	0.92
Kuroda et al. 2016 [79]	SFHx	4.9	11.8	23.8	8.7	21.6	43.3	10.4	14.1	22.1	0.63	0.82	0.88
	TM1	3.7	8.0	13.2	6.5	14.5	24.8	12.7	15.5	19.5	0.61	0.82	0.88
Kuroda et al. 2017 [80]	s11.2	2.5	7.7	15.9	4.8	14.3	29.0	10.0	12.7	21.3	0.82	0.90	0.93
	s15.0	2.7	6.7	11.7	5.0	12.2	20.5	11.2	14.3	19.5	0.75	0.89	0.92
Mezzacappa et al. 2020 [73]	c15-3D	1.8	4.4	7.4	3.0	8.2	14.0	17.0	21.1	33.8	0.42	0.69	0.82
Morozova et al. 2018 [81]	M10_LS220	NaN	1.3	5.2	NaN	2.4	9.5	16.2	21.7	NaN	0.47	0.72	0.81
	M10_DD2	NaN	1.9	7.4	NaN	3.4	13.7	15.2	19.6	NaN	0.57	0.80	0.85
	M13_SFHo	NaN	2.3	10.2	NaN	4.5	19.2	15.8	20.9	NaN	0.49	0.74	0.80
	M19_SFHo	NaN	3.9	16.7	NaN	6.9	30.0	18.9	24.4	NaN	0.37	0.68	0.78
Müller et al. 2012 [126]	L15-3	1.7	4.3	8.0	3.3	8.1	14.1	10.1	12.6	17.6	0.73	0.81	0.84
	N20-2	0.5	1.9	3.6	1.1	3.5	6.5	11.3	14.4	22.1	0.68	0.79	0.84
	W15-4	0.5	1.9	5.2	0.9	3.7	9.7	10.6	14.2	42.2	0.71	0.83	0.88
O'Connor&Couch 2018 [82]	mesa20	0.4	1.1	1.9	0.8	2.0	3.5	16.3	20.7	30.8	0.50	0.70	0.82
	mesa20_LR	0.6	1.4	2.6	1.0	2.5	4.7	18.5	25.0	42.3	0.45	0.67	0.79
	mesa20_pert	0.7	1.6	2.9	1.2	2.9	4.9	16.2	21.0	28.5	0.47	0.75	0.84
	mesa20_v_LR	0.4	1.1	1.9	0.8	2.1	3.5	16.0	20.2	29.6	0.51	0.78	0.87
Ott et al. 2013 [83]	s27-fheat1.00	2.4	5.8	10.5	4.3	10.8	20.2	11.1	14.3	20.1	0.75	0.89	0.92
	s27-fheat1.05	2.0	5.8	10.6	4.1	10.5	18.4	10.9	14.1	19.3	0.74	0.88	0.91
	s27-fheat1.10	2.4	5.8	10.0	4.0	10.0	17.4	11.2	14.2	19.6	0.75	0.88	0.92
	s27-fheat1.15	1.9	5.2	9.0	3.7	9.3	16.0	11.0	14.2	19.5	0.76	0.88	0.92
Powell&Müller 2019 [84]	s3.5_pns	1.8	3.9	6.4	3.2	7.1	11.7	17.0	20.9	30.4	0.44	0.75	0.83
	s18	3.2	7.7	12.7	5.5	14.0	23.0	15.5	19.2	28.0	0.47	0.73	0.81
Powell&Müller 2020 [85]	m39	10.3	30.7	70.2	18.5	56.6	128.8	12.8	18.8	38.2	0.57	0.73	0.81
	s18np	2.3	5.7	12.3	4.1	10.5	22.7	10.6	14.6	21.5	0.67	0.81	0.88
	y20	3.4	8.5	14.6	6.2	15.5	26.8	16.2	19.9	29.4	0.42	0.72	0.82
Radice et al. 2019 [50]	s9	0.0	0.4	0.7	0.2	0.7	1.3	11.1	14.3	23.1	0.73	0.84	0.91
	s13	0.4	1.0	1.8	0.7	1.8	3.1	10.9	14.3	21.1	0.68	0.80	0.87
	s25	2.4	5.6	9.4	4.3	10.3	17.7	22.5	30.6	42.8	0.43	0.65	0.78
Richers et al. 2017 [86]	A467_w0.50_SFHx	NaN	8.0	32.9	NaN	15.1	60.6	8.70	13.7	NaN	0.86	0.91	0.93
	A467_w0.50_LS220	NaN	10.3	43.0	NaN	18.1	80.3	10.2	14.2	NaN	0.85	0.93	0.94
	A467_w9.50_SFHx	NaN	24.2	105.2	NaN	47.9	194.2	10.3	14.3	NaN	0.82	0.91	0.91
	A467_w9.50_LS220	NaN	22.5	90.5	NaN	40.8	171.9	10.1	14.1	NaN	0.82	0.89	0.92
Scheidegger et al. 2010 [54]	R1E1CA_L	0.4	1.3	3.5	0.8	2.4	6.5	9.9	13.1	22.5	0.76	0.86	0.91
	R3E1AC_L	29.9	89.6	171.8	55.5	163.9	313.9	10.6	13.4	17.2	0.76	0.89	0.93
	R4E1FC_L	31.8	98.4	203.4	59.3	180.1	374.6	8.9	11.8	15.7	0.81	0.91	0.94
Yakunin et al. 2015 [72]	B12	NaN	3.6	13.6	NaN	6.6	25.2	15.2	19.3	NaN	0.51	0.80	0.88
	B15	NaN	4.3	17.9	NaN	7.7	32.4	17.4	22.1	NaN	0.44	0.78	0.87
	B20	NaN	3.0	15.2	NaN	5.7	28.2	15.8	22.2	NaN	0.52	0.82	0.89
	B25	NaN	6.6	26.1	NaN	12.5	48.2	15.7	20.9	NaN	0.49	0.76	0.85

Detection range of GW at O5
(PSD BNS range LIGO: 330Mpc, Virgo 150Mpc, KAGRA 130Mpc)

Neutrino-driven mechanism: ~ 10kpc

Rapidly rotating progenitor case: ~100kpc

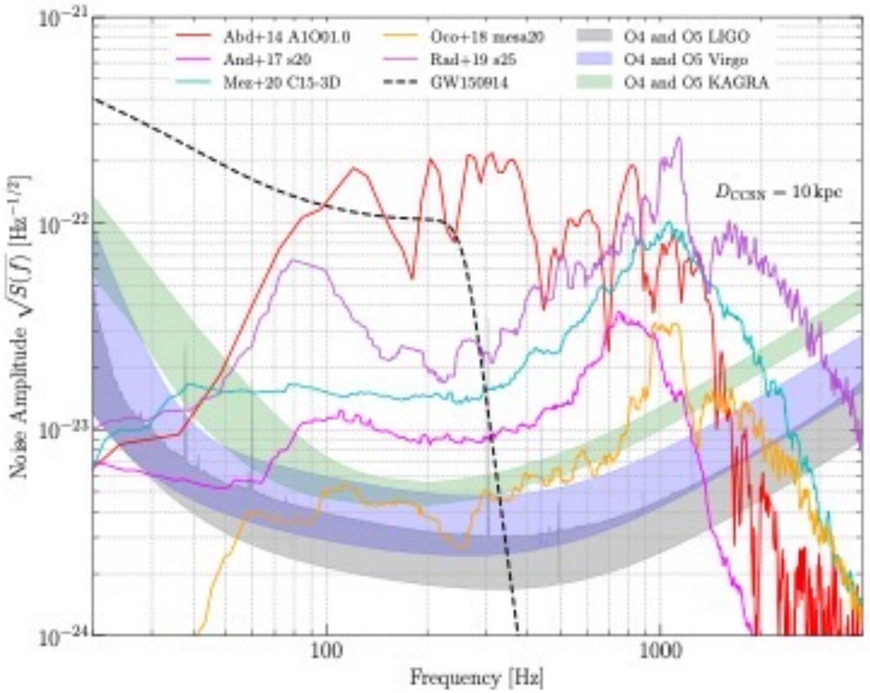

Sky localization accuracy for burst signals

Essick et al. arXiv:1409.2435

Area (in square degrees) that must be searched before the injected test signal can be found.

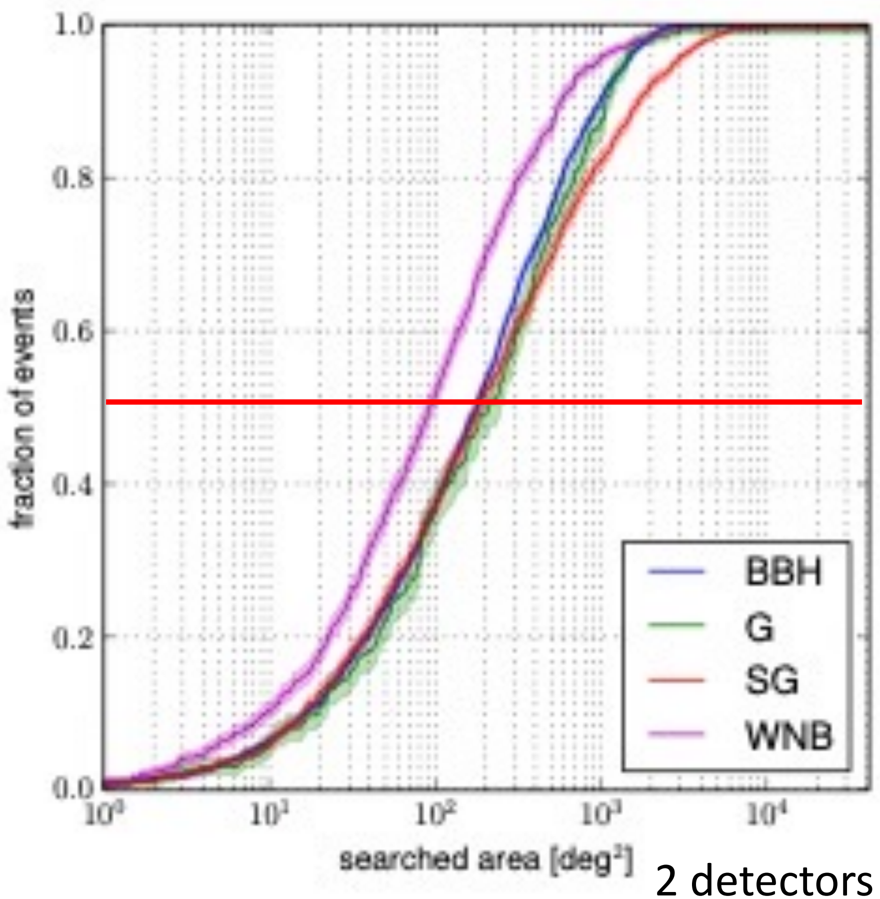

2 detectors

(a) cWB HL 2015

100-200 square degree

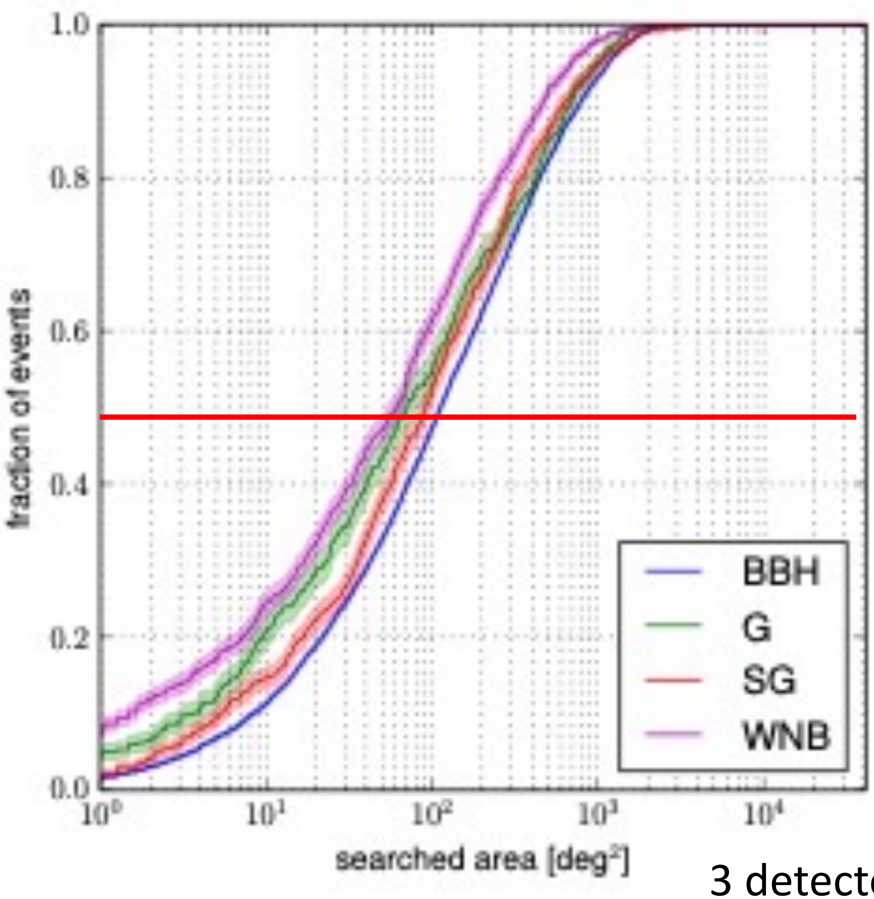

3 detectors

(b) cWB HLV 2016

60-110 square degree

Supernovae

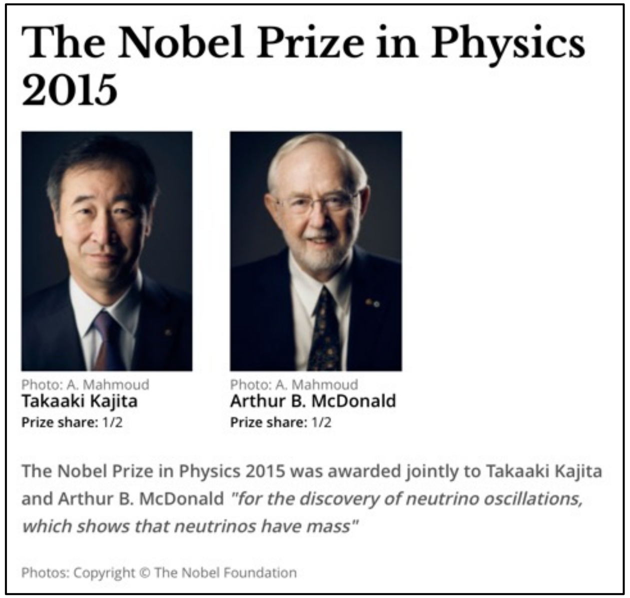
The Nobel Prize in Physics 2015

Photo: A. Mahmoud
Takaaki Kajita
Prize share: 1/2

Photo: A. Mahmoud
Arthur B. McDonald
Prize share: 1/2

The Nobel Prize in Physics 2015 was awarded jointly to Takaaki Kajita and Arthur B. McDonald *"for the discovery of neutrino oscillations, which shows that neutrinos have mass"*

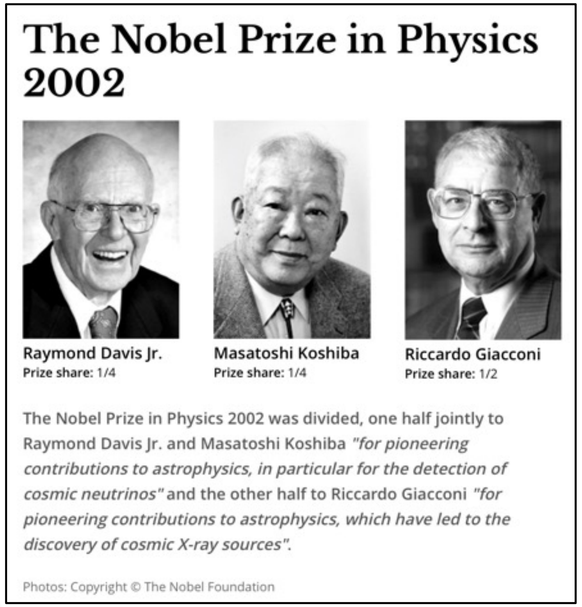
The Nobel Prize in Physics 2002

Raymond Davis Jr.
Prize share: 1/4

Masatoshi Koshiba
Prize share: 1/4

Riccardo Giacconi
Prize share: 1/2

The Nobel Prize in Physics 2002 was divided, one half jointly to Raymond Davis Jr. and Masatoshi Koshiba *"for pioneering contributions to astrophysics, in particular for the detection of cosmic neutrinos"* and the other half to Riccardo Giacconi *"for pioneering contributions to astrophysics, which have led to the discovery of cosmic X-ray sources"*.

Neutrino

Gravitational waves

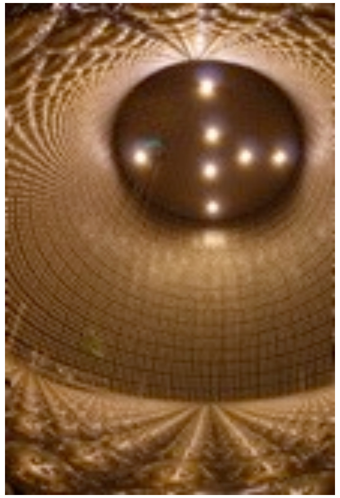

SuperKamiokande

Coincident observation to explore explosion mechanism.
Detectors in ICRR can contribute a lot for such a case.

KAGRA

This is possible if a supernova occurs near the Galaxy (once in ~50 years)

Binary neutron star mergers

About 90 compact binary mergers have been detected!

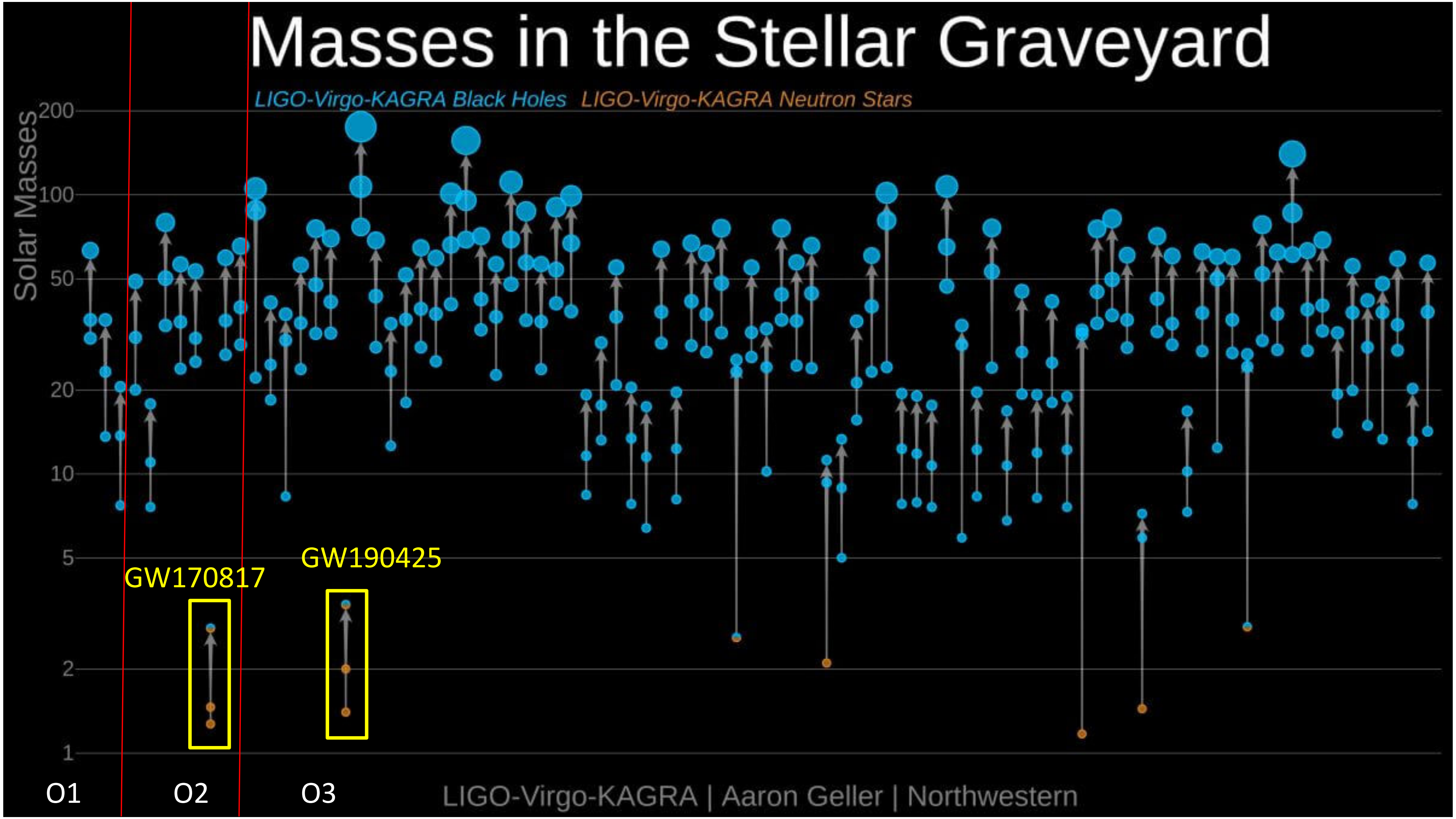

Historical BNS merger GW170817

Coincident detection of GRB and GW

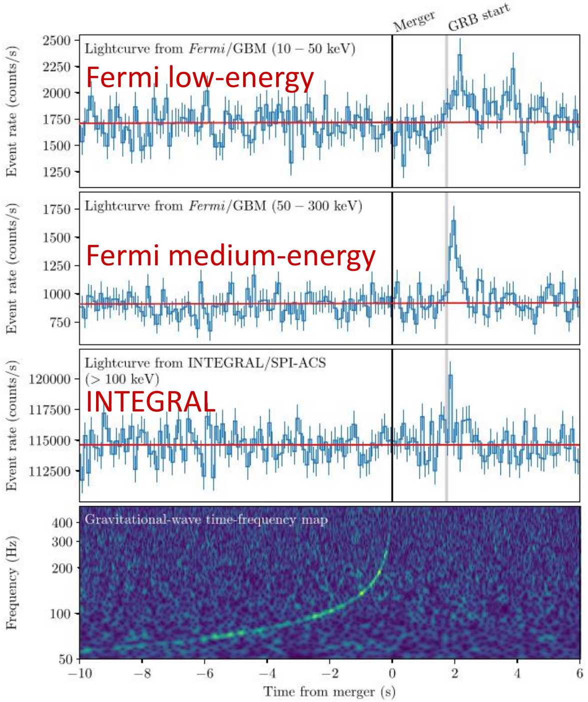

3 detectors

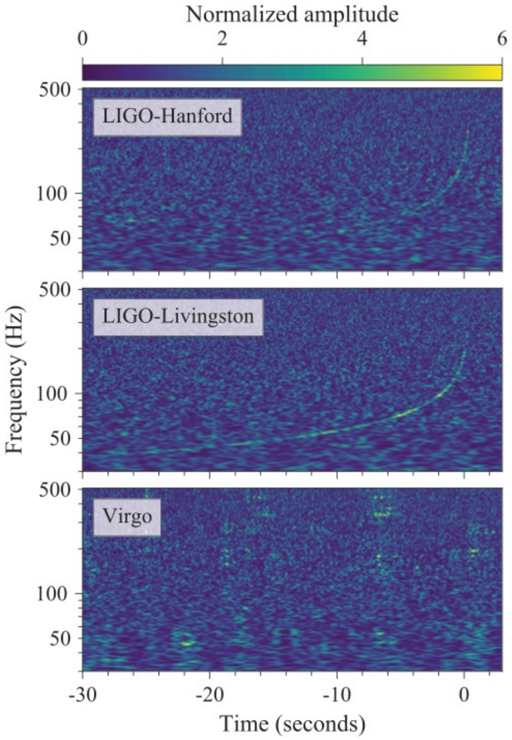

PRL 119, 161101 (2017)

Optical counterparts

The Astrophysical Journal Letters, 848:L12 (59pp), 2017 October 20 Abbott et al.

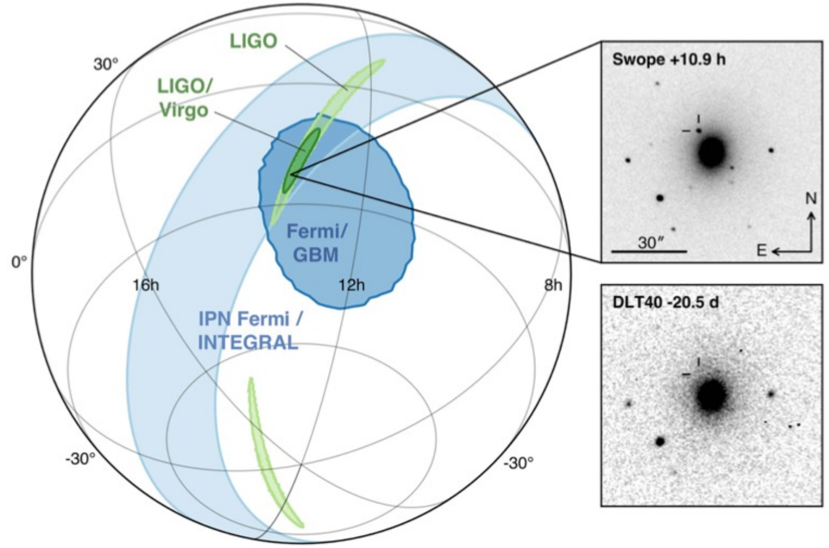

Figure 1. Localization of the gravitational-wave, gamma-ray, and optical signals. The left panel shows an orthographic projection of the 90% credible regions from LIGO (190 deg^2; light green), the initial LIGO-Virgo localization (31 deg^2; dark green), IPN triangulation from the time delay between *Fermi* and *INTEGRAL* (light blue), and *Fermi*-GBM (dark blue). The inset shows the location of the apparent host galaxy NGC 4993 in the Swope optical discovery image at 10.9 hr after the merger (top right) and the DLT40 pre-discovery image from 20.5 days prior to merger (bottom right). The reticle marks the position of the transient in both images.

Sky location consisitent

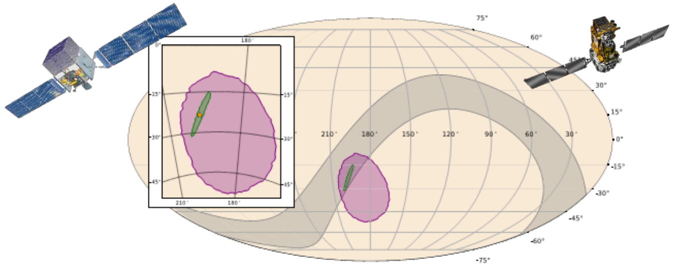

Kilonova
Aftergrow
r-process nucleosynthesis
Hubble parameter (70+12-8 km/s/Mpc)

Source localization accuracy for two BNS signals

Sky map for GW170817 (O2) (green region)

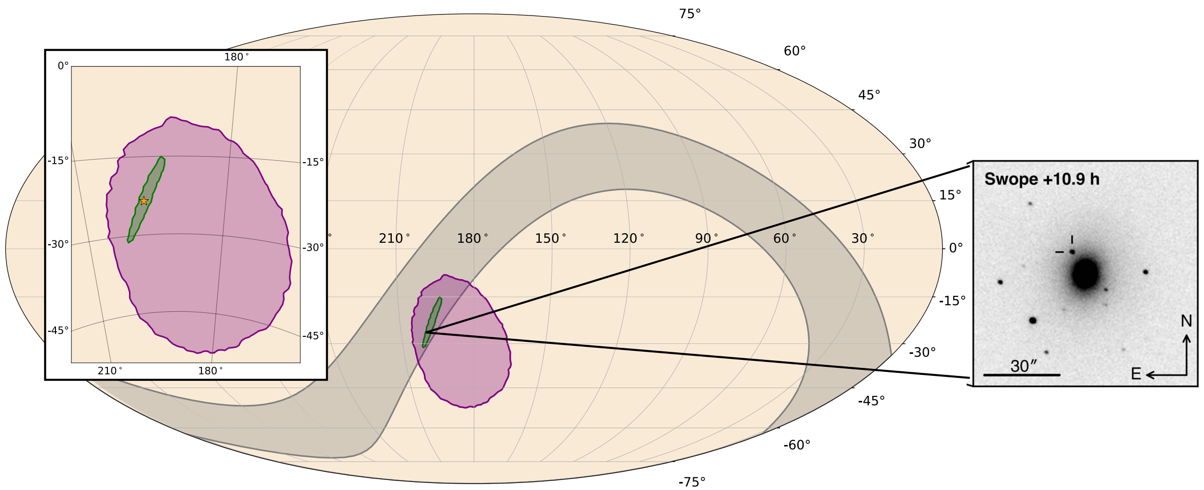

Sky map for GW190425 (O3)

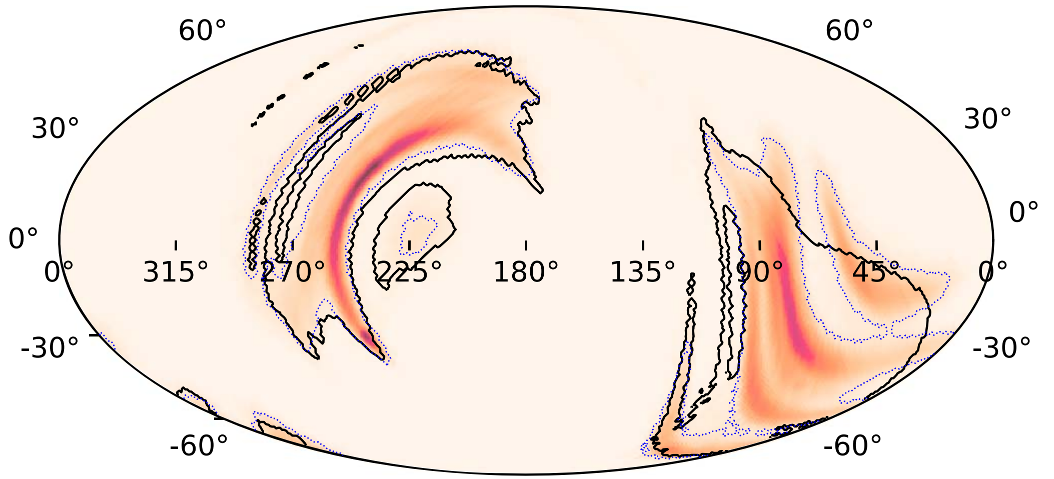

- Sky map: error region of source location (possible location of the source in the sky)
- Initial sky map ～ 30 square degree
  - 3 detector observation
- Distance ～ 40 Mpc

- Initial sky map ～ 10,000 square degree
  - 2 detector observation with LIGO-Livingston and Virgo (Hanford was offline)
- Estimated distance ～ 159 Mpc
  - EM signals should have been fainter even if they were emitted

Confident BNS in O3: GW190425

BNS event detected strongly by LIGO Livingston, and weakly by Virgo (LIGO Hanford was off at the time)

Table 1
Source Properties for GW190425

	Low-spin Prior ($\chi < 0.05$)	High-spin Prior ($\chi < 0.89$)
Primary mass m_1	1.60–1.87 $M_\odot$	1.61–2.52 $M_\odot$
Secondary mass m_2	1.46–1.69 $M_\odot$	1.12–1.68 $M_\odot$
Chirp mass $\mathcal{M}$	$1.44^{+0.02}_{-0.02}$ $M_\odot$	$1.44^{+0.02}_{-0.02}$ $M_\odot$
Detector-frame chirp mass	$1.4868^{+0.0003}_{-0.0003}$ $M_\odot$	$1.4873^{+0.0008}_{-0.0006}$ $M_\odot$
Mass ratio m_2/m_1	0.8 – 1.0	0.4 – 1.0
Total mass $m_{\rm tot}$	$3.3^{+0.1}_{-0.1}$ $M_\odot$	$3.4^{+0.3}_{-0.1}$ $M_\odot$
Effective inspiral spin parameter $\chi_{\rm eff}$	$0.012^{+0.01}_{-0.01}$	$0.058^{+0.11}_{-0.05}$
Luminosity distance $D_{\rm L}$	159^{+69}_{-72} Mpc	159^{+69}_{-71} Mpc
Combined dimensionless tidal deformability $\tilde{\Lambda}$	$\leqslant 600$	$\leqslant 1100$

~ 10,000 deg^2

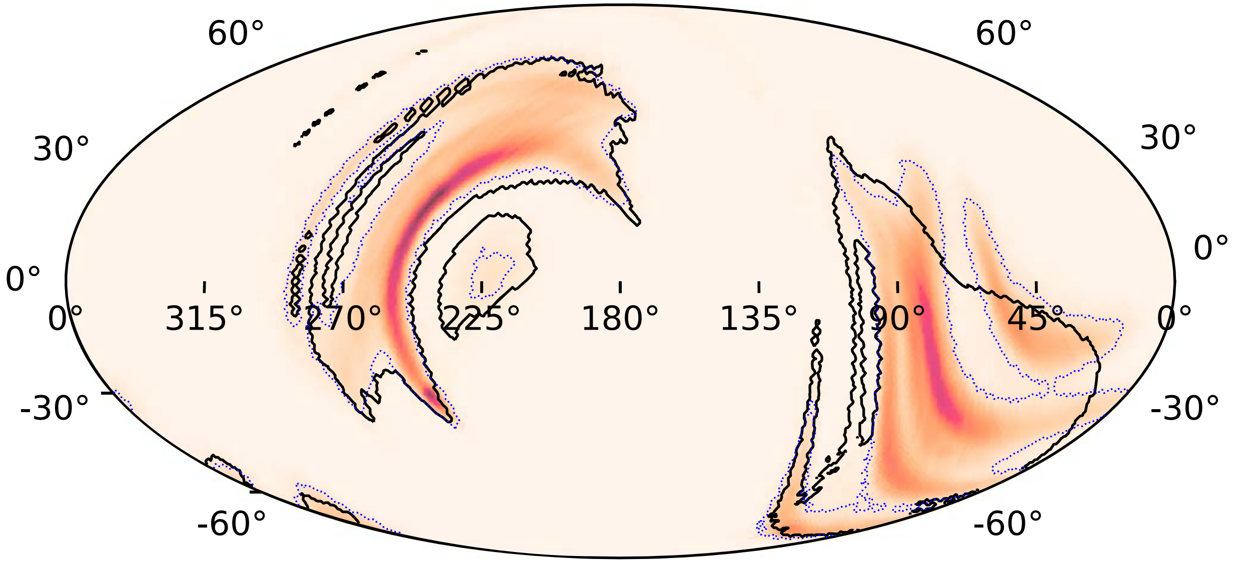

Figure 2. Sky map for GW190425. The shaded patch is the sky map obtained from the Bayesian parameter estimation code LALINFERENCE (Veitch et al. 2015) (see Section 4) with the 90% confidence region bounded by the thin dotted contour. The thick solid contour shows the 90% confidence region from the low-latency sky localization algorithm BAYESTAR (Singer & Price 2016).

- Estimated distance ~ 159 Mpc
- EM signals should have been fainter even if they were emitted
- No clear EM counterpart was identified.

Source localization with GW detectors

- It is important to determine the location of the source accurately so that astronomical telescopes can perform follow-up observation to search for optical counterpart.
- One laser interferometer can not determine the location of short duration sources in the sky.
- Signals from different direction are received with the detector in the same way, and can not be distinguished.

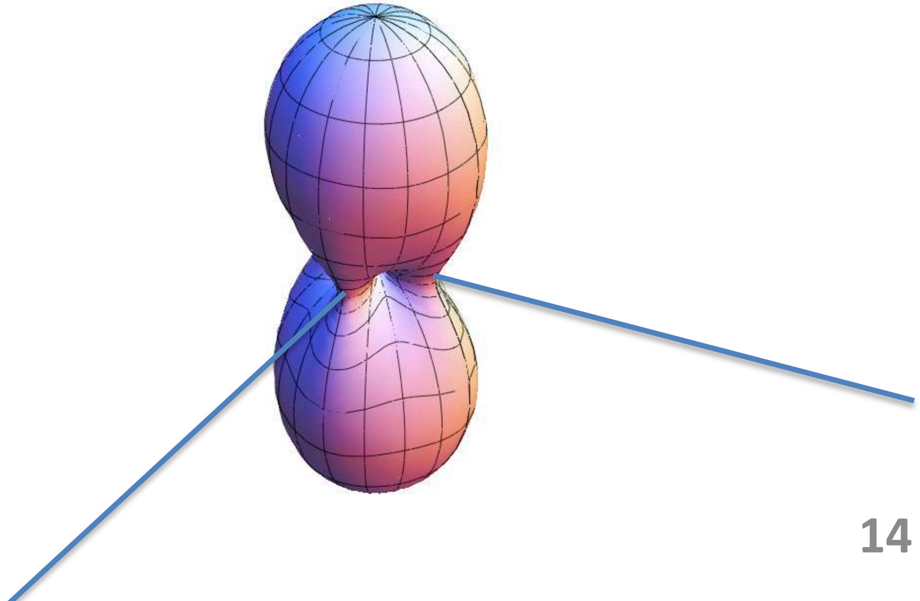

Source localization with GW detectors

- We need 3 or more detectors to detemine the source location accurately

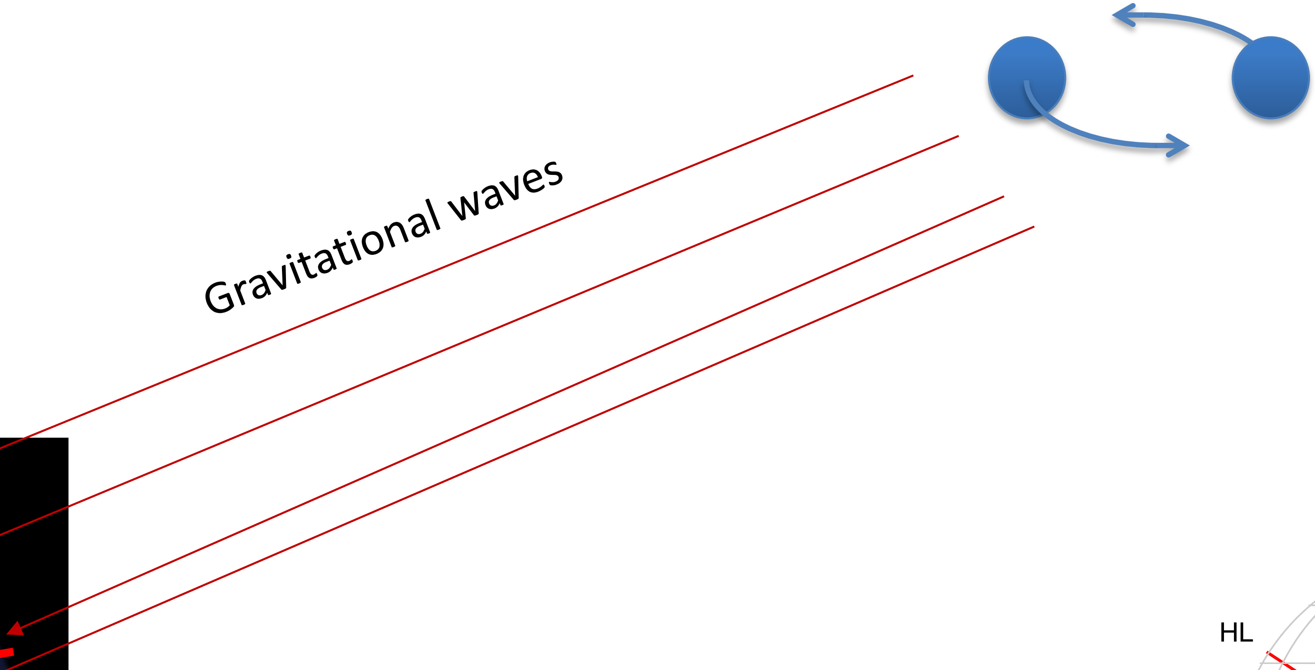

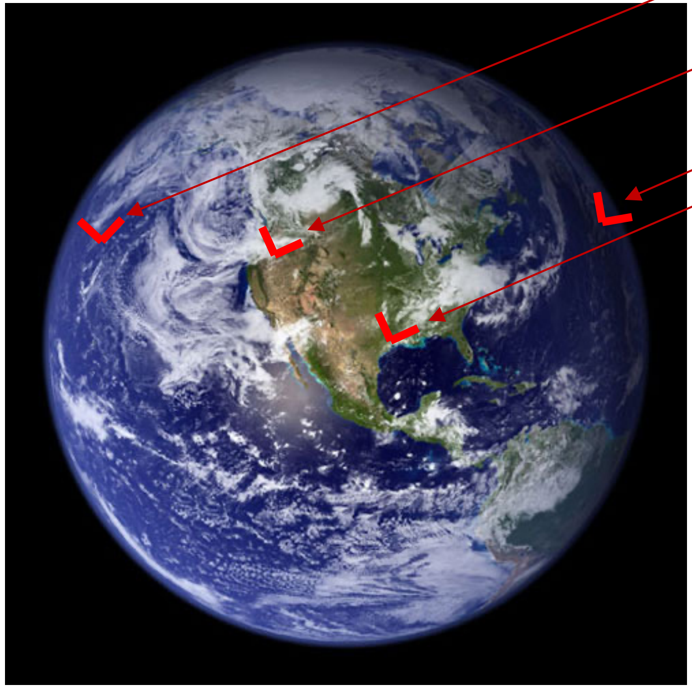

Arrival time of signal at each detector is different and the difference depends on the location in the sky.
With 3 or more detectors, the direction to the source can be determined.

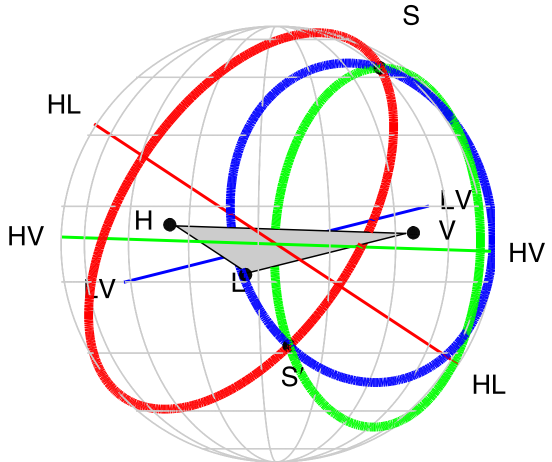

KAGRA O4 and later

- The next LIGO-Virgo-KAGRA observing run (O4) is planned to start in mid-December 2022.
- KAGRA will join O4 from the beginning.

- Upgrade works toward O4 is in progress.

- Expected sensitivity of KAGRA at O4 is still not so great compared to LIGO-Virgo.

  Expected binary neutron star detection range (ref. https://gwcenter.icrr.u-tokyo.ac.jp/en/archives/1581)
  LIGO: 160 - 190 Mpc
  Virgo: 80 - 115 Mpc
  KAGRA: 1 - 10 Mpc

- But we will continue our effort to achive better sensitivity, and toward the design sensitiviy

Source localization

Assumed sensitivity (BNS range)
LIGO 120Mpc, Virgo 60Mpc, KAGRA 25Mpc

Ref: GW170817: 28-31 deg^2

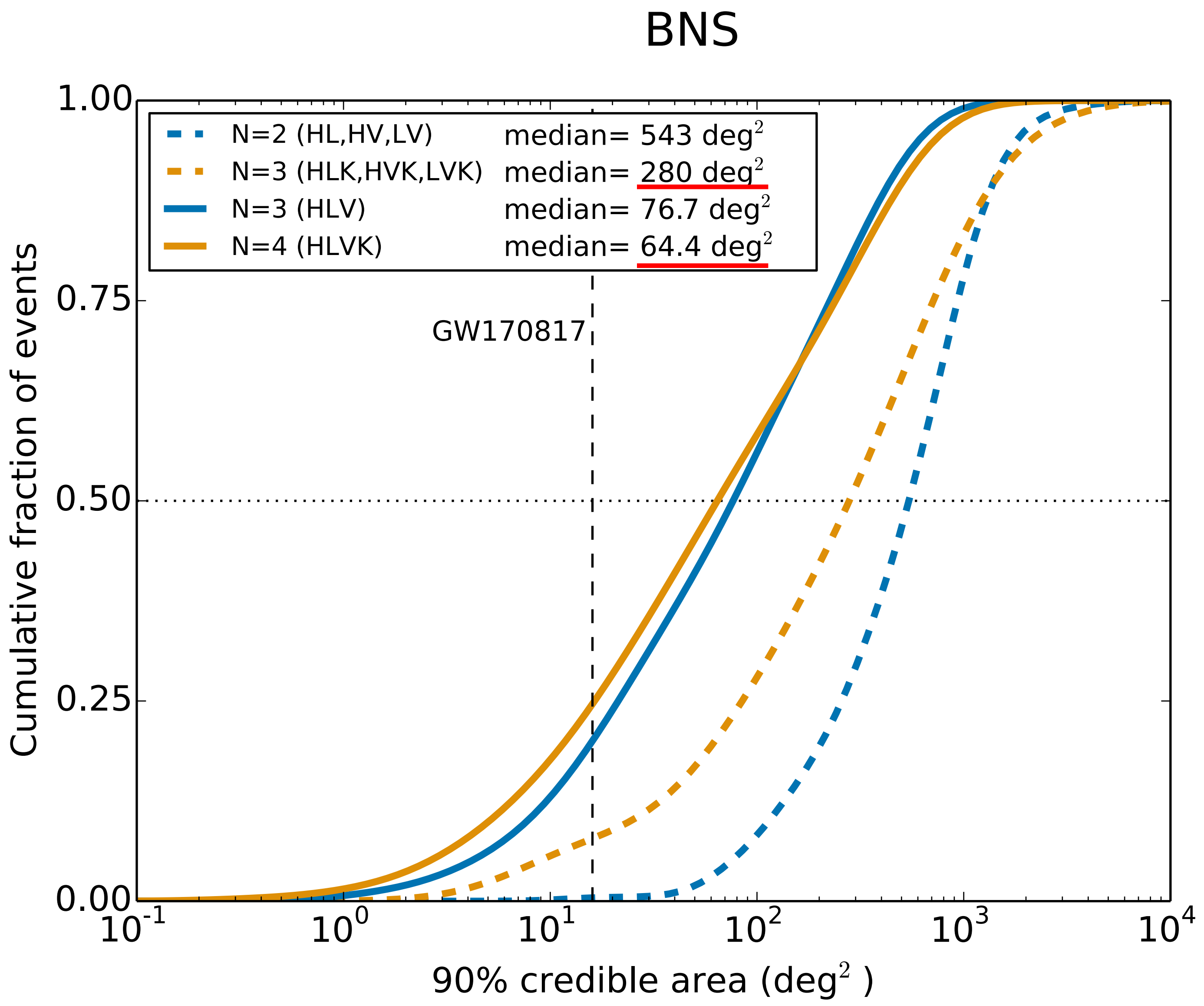

Sky localization accuracy

At design sensitivity

NS-NS @180Mpc (95%CI)

(1.4,1.4)Msun	LHV	LHVK
median of δΩ [Deg^2]	30.25	9.5

J.Veitch et al., PRD85, 104045 (2012)
(Bayesian inference)
See also Rodriguez et al. 1309.3273

L:LIGO-Livingston
H:LIGO-Hanford
V: Virgo
K: KAGRA
I: LIGO-India

Ref: GW170817: 28-31 deg^2 @ 40 Mpc

BH-NS @200Mpc

(10,1.4)Msun	LHV	LHVK	LHVKI
median of δΩ [Deg^2]	21.5	8.44	4.86

(Tagoshi, Mishra, Arun, Pai, PRD90, 024053 (2014) , Fisher matrix)

Low latency alert

Low latency alert

R. Magee et al. ApJ L. 910, L21 (2021)

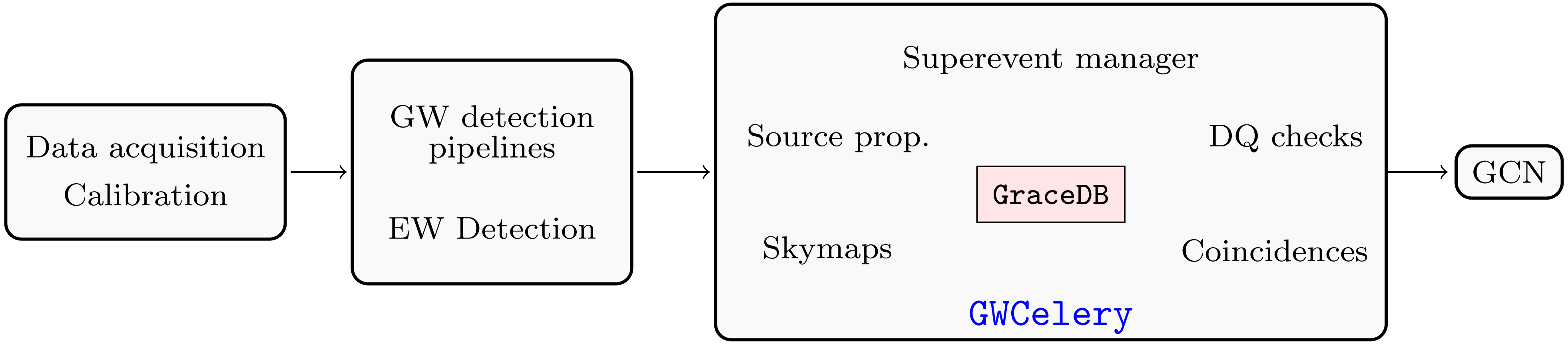

GW170817 alert latency
Alert: ~40 min., Sky map: ~5 hrs

O3: autonomous preliminary GCN Notice started
Preliminary GCN Notice latency: 7.0^{+92}_{-4} minutes
(automated process could not work for several cases)

Low latency alert

R. Magee et al. ApJ L. 910, L21 (2021)

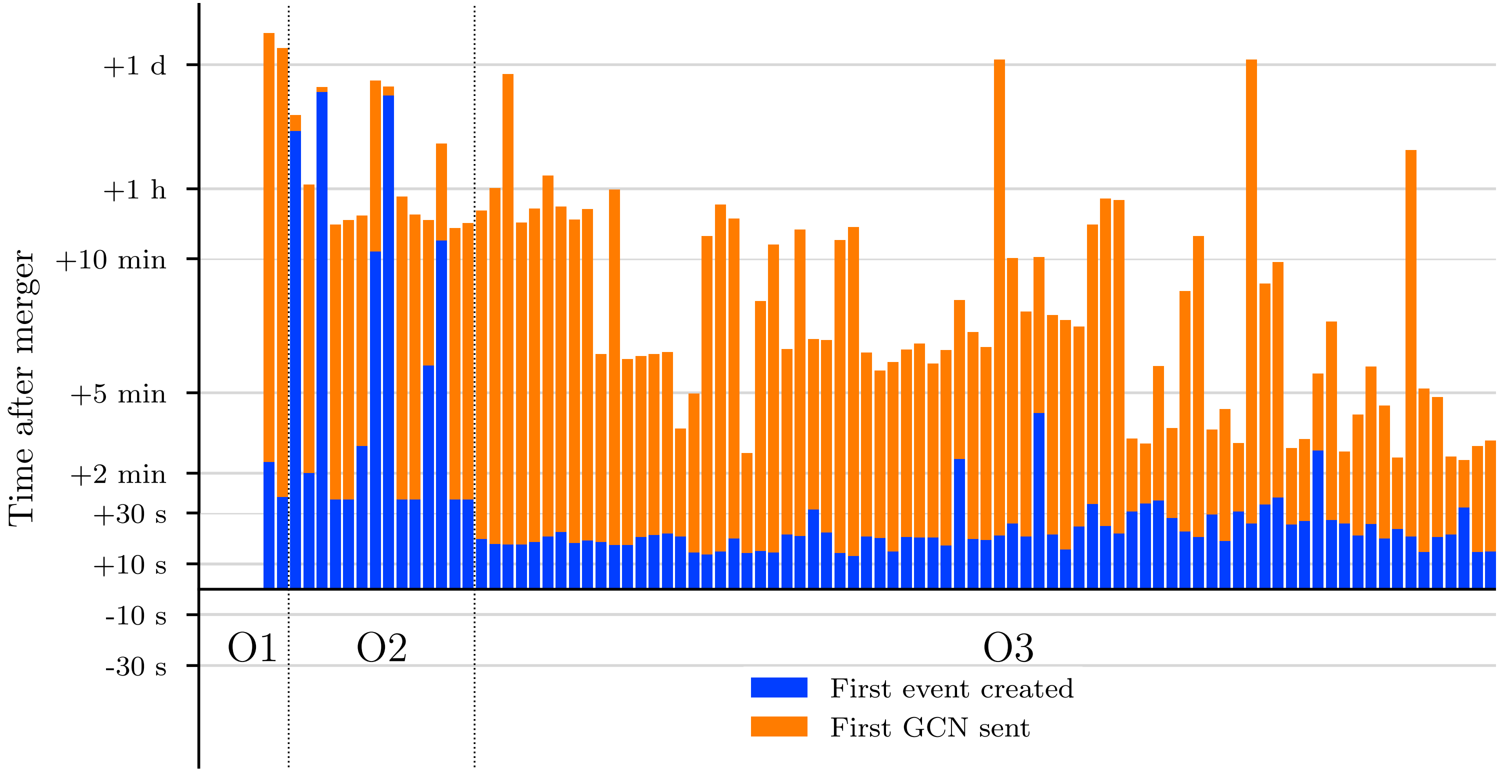

GW170817 alert latency
Alert: ~40 min.,   Sky map: ~5 hrs

O3: autonomous preliminary GCN Notice started
Preliminary GCN Notice latency: 7.0^{+92}_{-4} minutes
(automated process could not work for several cases)

Early warning (pre-merger) alert

R. Magee et al. ApJ L. 910, L21 (2021)

A BNS signal stays in the detector's band width for ~1 minute to 10 minutes
(it depend on the lowest cutoff frequency)

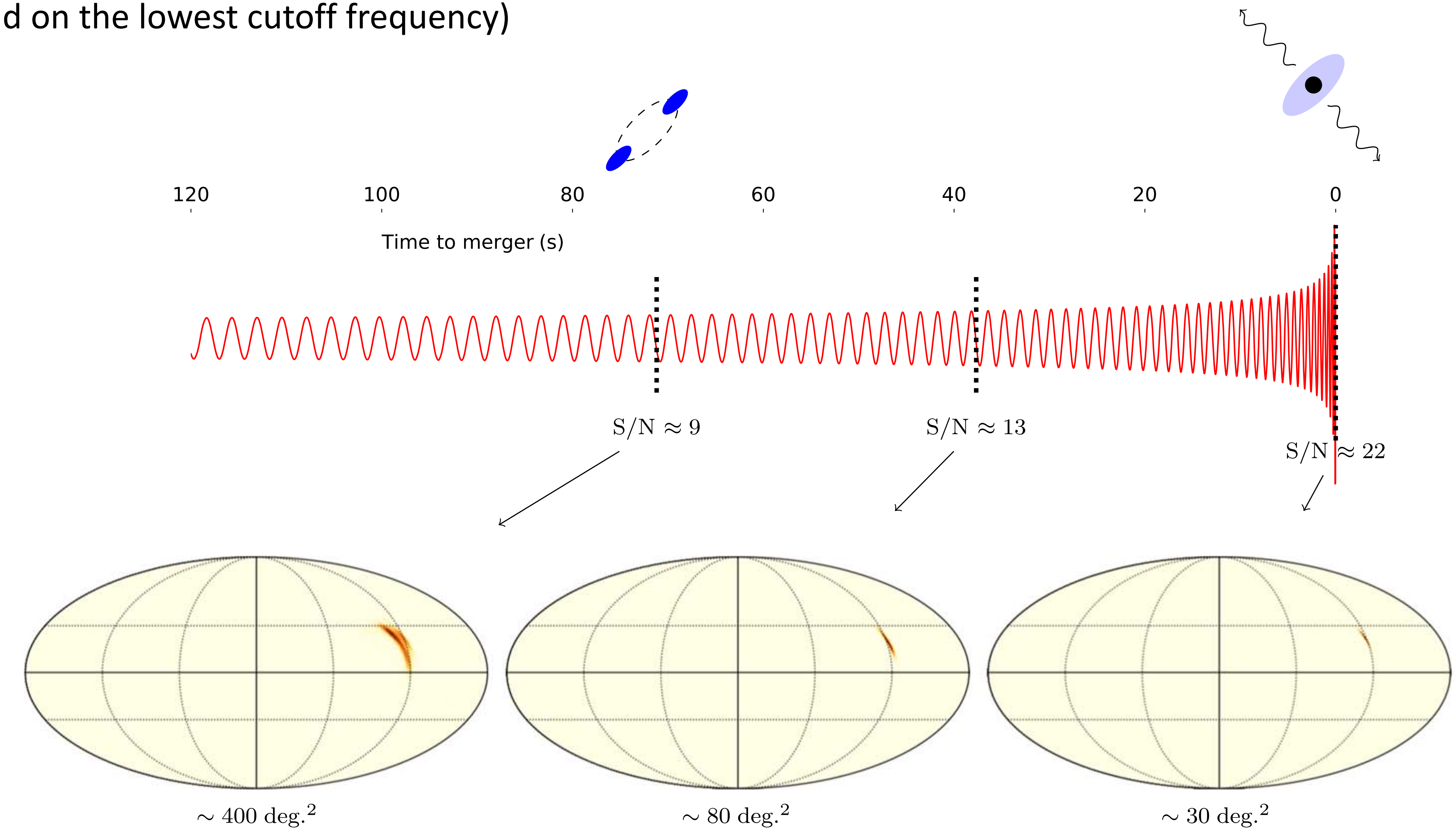

Early warning (pre-merger) alert

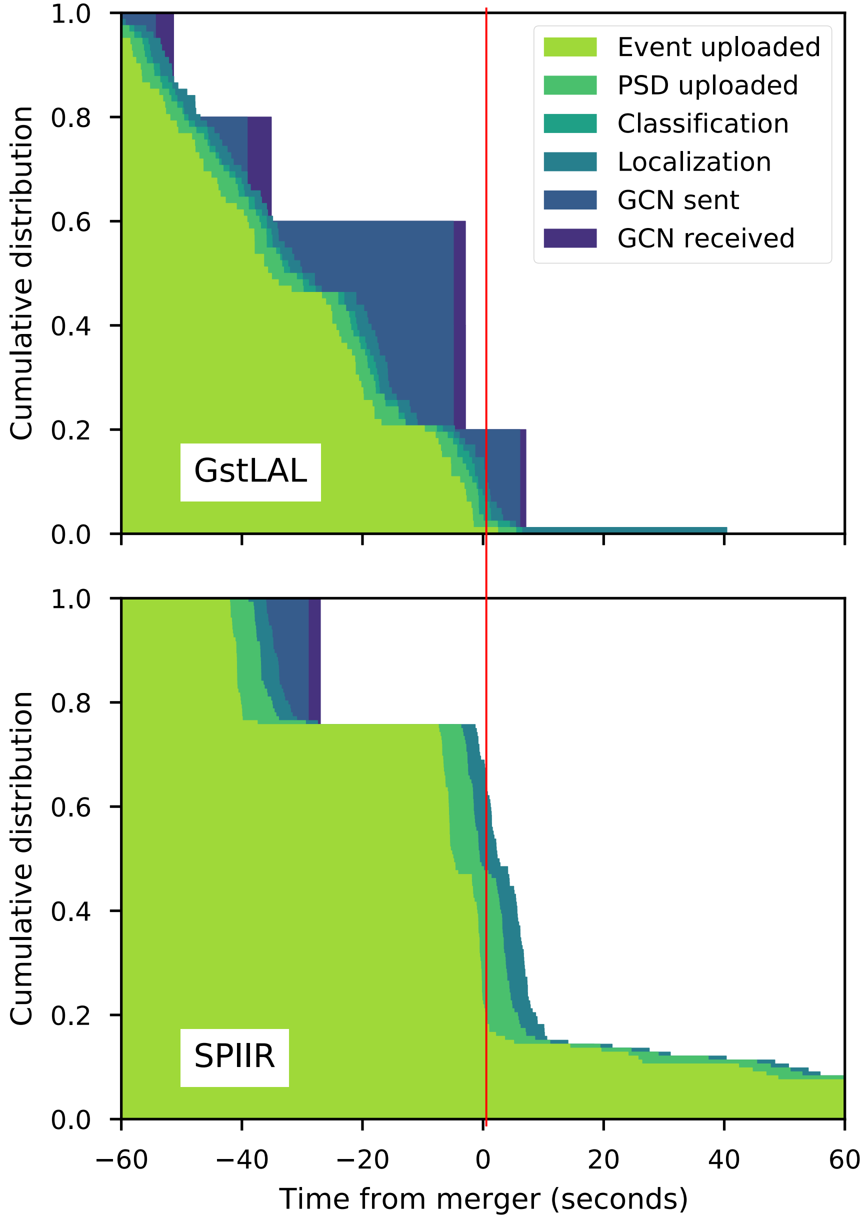

R. Magee et al. ApJ L. 910, L21 (2021)

Mock data challenge of early warning alert by using LV O3 data about 8 days

How early BNS trigger information can be uploaded to GraceDB before merger time

~85% (GstLAL)
~35% (SPIIR) could be done before merger

Early warning (pre-merger) alert

R. Magee et al. ApJ L. 910, L21 (2021)

Mock data challenge of early warning alert by using LV O3 data about 8 days

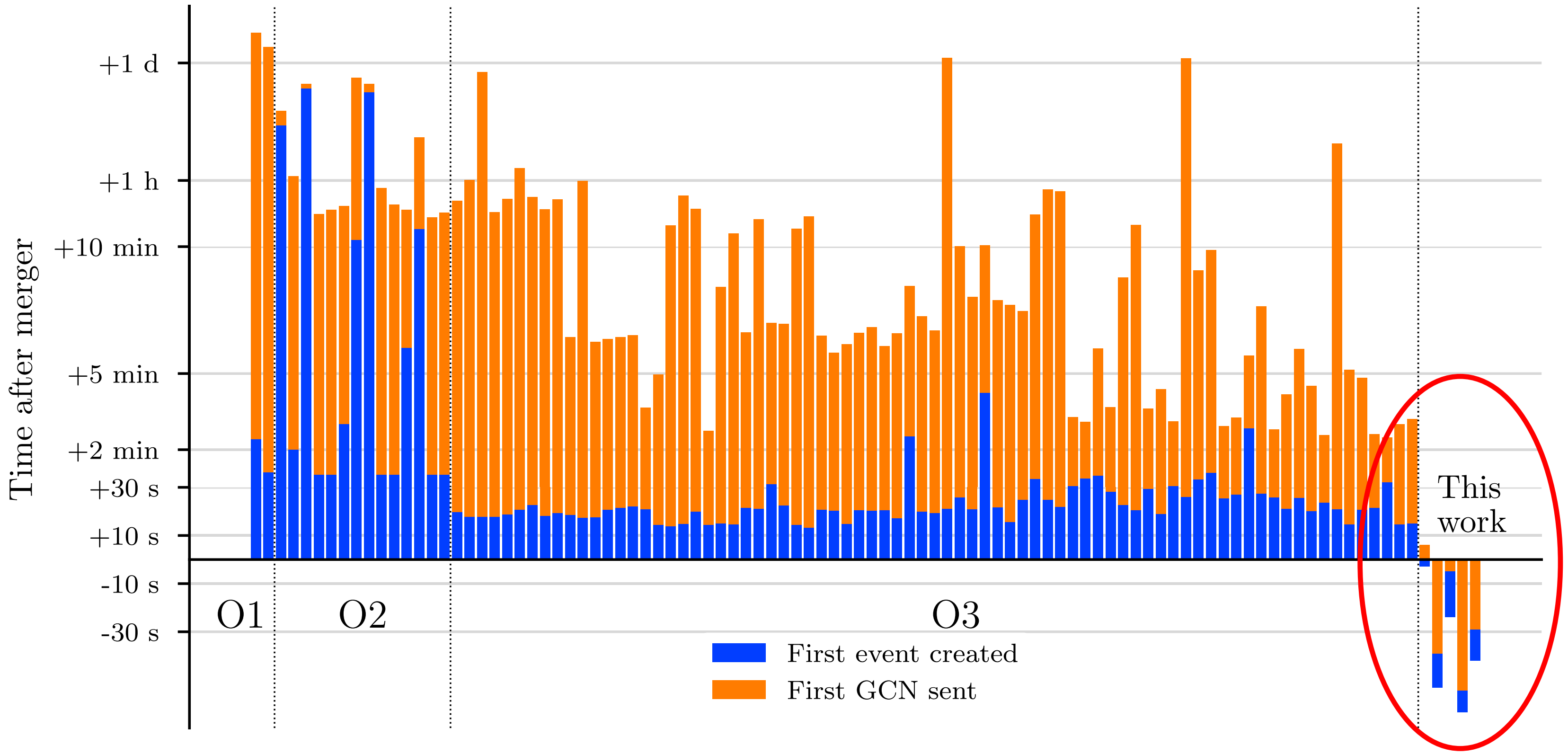

5 trigger satisfy alert sending criteria

4 trigger could be sent out before merger

Sky map and parameter estimation

GW190425

Initial sky map by BAYESTAR: 10,200 deg^2 (90% credible region)

Improved sky map using a Bayesian analysis: 8,284 deg^2 (90% credible region)

BAYESTAR ~ a few seconds,

It takes time to obtain an improved sky map with full Bayesian analysis (>hours)

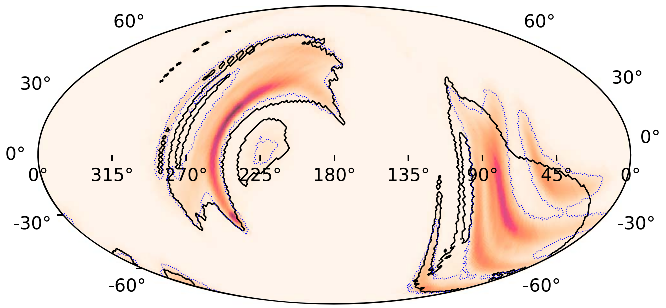

Figure 2. Sky map for GW190425. The shaded patch is the sky map obtained from the Bayesian parameter estimation code LALINFERENCE (Veitch et al. 2015) (see Section 4) with the 90% confidence region bounded by the thin dotted contour. The thick solid contour shows the 90% confidence region from the low-latency sky localization algorithm BAYESTAR (Singer & Price 2016).

Sky map and parameter estimation

Efforts to reduce the computation time

- Morisaki, Raymond (PRD102, 104020 (2020)) take into account of information from detection pipelines
- Morisaki (PRD104, 044062 (2021)) Divide frequency range of signal
- Eunsub, Morisaki, Tagoshi, 2203.05216, Use another parameters for masses and spins

- Sky map generation with machine learning

Chatterjee et al. (PRD100, 103025 (2019))
Sasaoka et al. 2202.12784

Sky map generation with machine learning

Test result demonstration on 3-detector signal with simulated noise

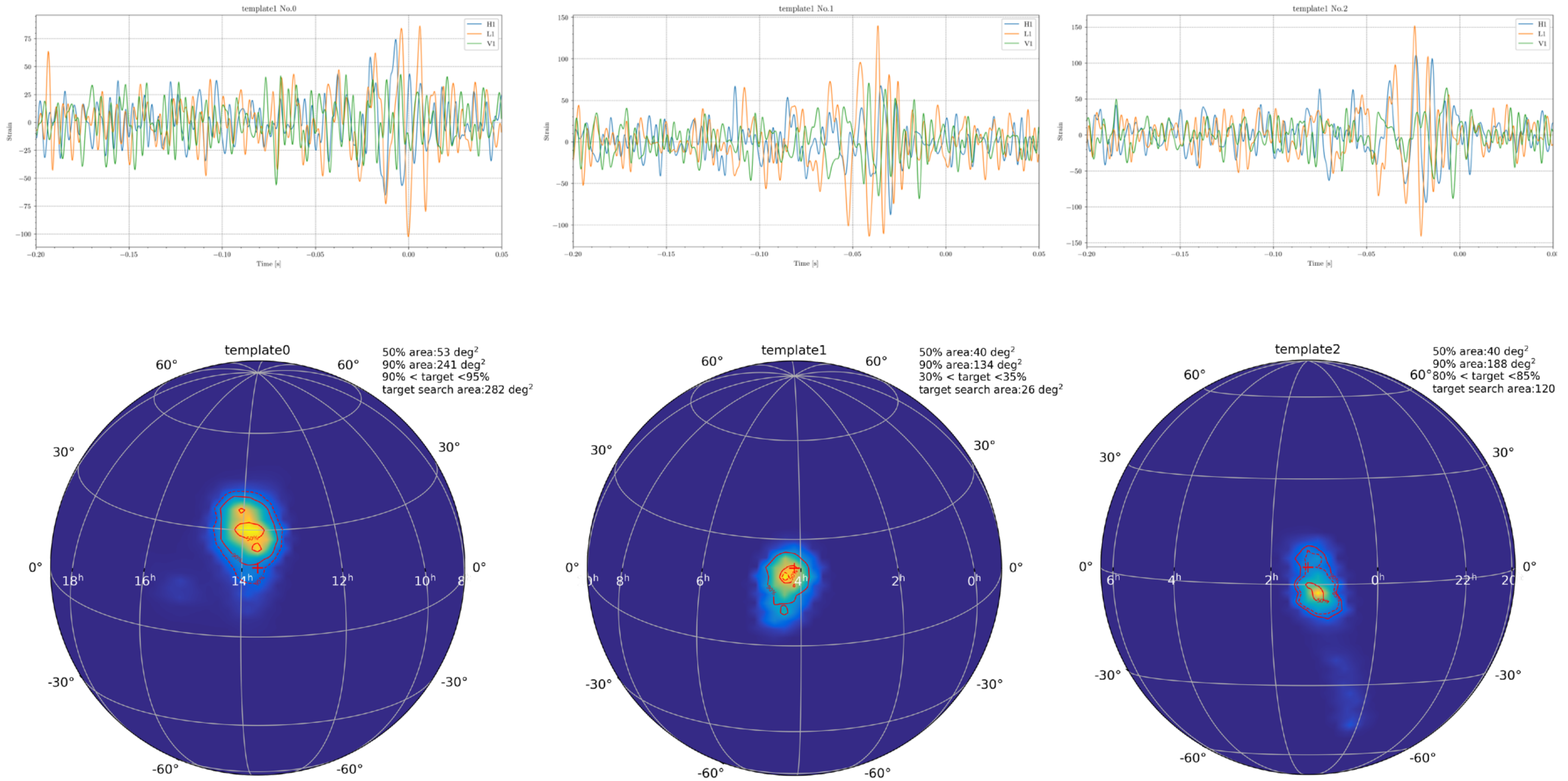

Summary

- Core collapse supernovae GW can be detected within ~10kpc, and within ~100kpc for rapidly rotating progenitors
- Sky localization accuracy of supernova signals may not be very good

- For better sky localization, we need observation with 3 or more detectors.
- Since the ducy cycle of each detector is < 90%, there are time when one or more detectors are down.
- In order to increase the observing time with 3 detectors, we need KAGRA.

- Low latency alerts to GCN have been issued.
- Efforts are ongoing to reduce the latency of alert and to obtain accurate sky map earlier.

- Development and testing of early warning (pre-merger) alert are ongoing.
- It is better to improve the sensitivity at lower frequency of detectors to obtain better S/N and better sky localization accuracy form early warning alert.
- Upgraded LIGO/Virgo/KAGRA or 3rd generation detectors may be needed.

Appendix

Early warning (pre-merger) alert

R. Magee et al. ApJ L. 910, L21 (2021)

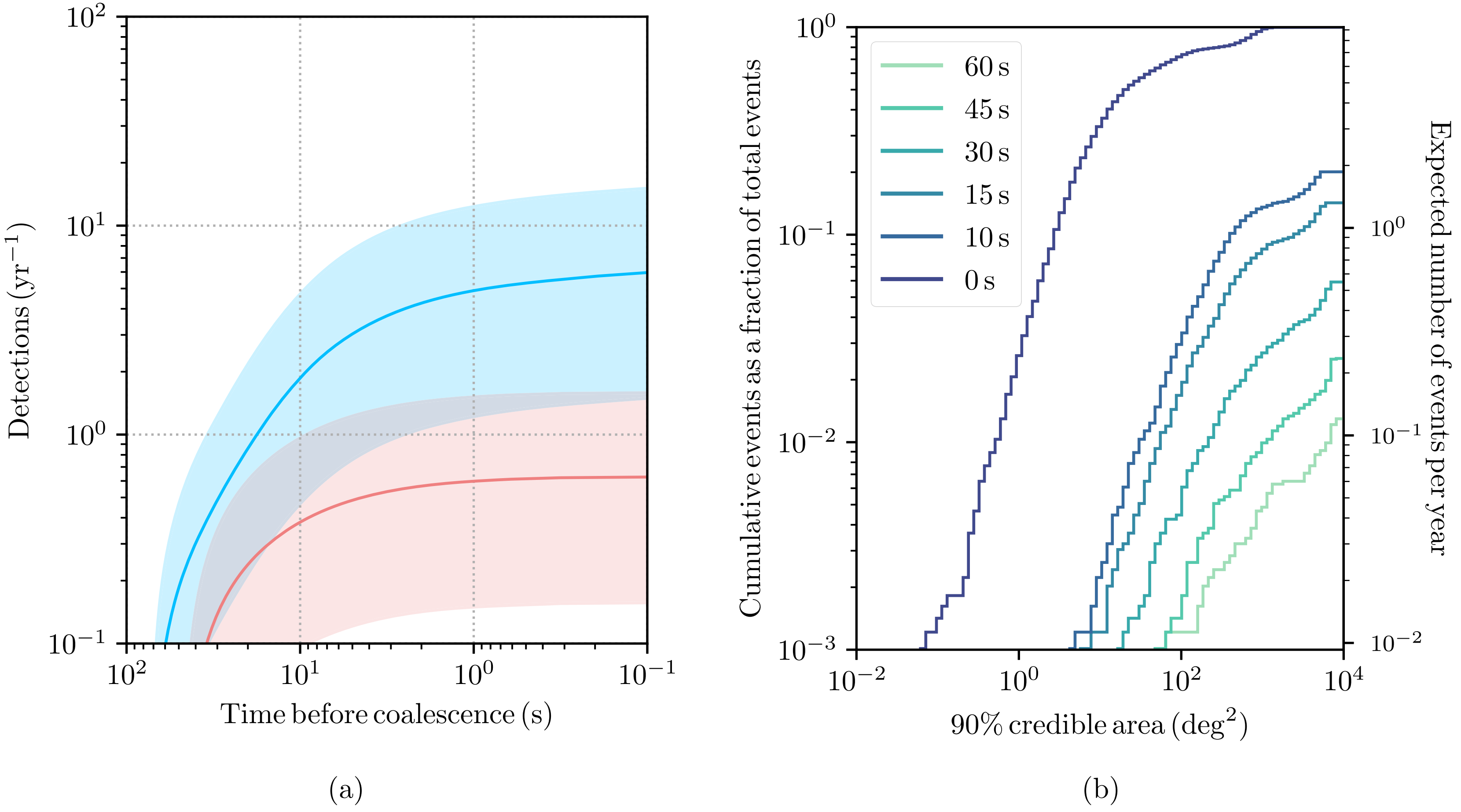

Figure 4. (a) Projected O4 early warning detection rate assuming 0 s (blue) and 25 s (red) end-to-end latencies from the GW alert system. The worst case scenario assumes 5 s for calibration and data transfer, 5 s for pipeline analysis, and 15 s for event upload and GCN creation. The rate of expected detections was estimated from a simulated data set assuming a 100% detector duty cycle for the 4-detector HLVK network. The uncertainty bands reflect the (5%, 95%) confidence region for the BNS rate. Signals with network S/Ns greater than 12 are considered recovered. (b) The expected localization distribution for BNS detections at six approximate early warning times. No latencies are included in this figure. The inclusion of an end-to-end latency does not shift the histogram itself; the labeled times before merger would all systematically shift instead. Both plots use the BNS rates estimated in Abbott et al. (2020b).